Materials Research Bulletin 160 (2023) 112130

Contents lists available at ScienceDirect

Materials Research Bulletin

journal homepage: www.elsevier.com/locate/matresbu

Research Papers

A facile one-pot synthesis of phyto-conjugate superparamagnetic magnetite nanoparticles for the rapid removal of hexavalent chromium from water bodies

Julia Garvasis [a], Anupama R. Prasad [a], K.O. Shamsheera [a], T.A. Nidheesh Roy [b], Abraham Joseph [a,*]

[a] Department of Chemistry, University of Calicut, Calicut University, P O-673 635, India
[b] Department of Biotechnology, University of Calicut, Calicut University, P O, 673 635, India

ARTICLE INFO

Keywords:
CMNs
Adsorptive removal
Chromolaena odorata
Superparamagnetic

ABSTRACT

Sustainable and economical strategies for producing efficacious adsorbent systems for the rapid removal of hazardous Cr(VI) have recently gained research attention. This study employs the aqueous extract of *Chromolaena odorata* flowers as a green reductant and capping agent for the synthesis of Chromolaena odorata-derived magnetite nanoparticles (CMNs). The method yielded relatively monodispersed and small superparamagnetic magnetite nanoparticles with an average particle size of 3.14±0.25 nm. At an optimum pH of 2, CMNs enabled rapid removal of Cr(VI) and its subsequent reduction to Cr(III) in under 10 minutes. The maximum adsorption capacity recorded was 173.12 mg g^{-1}. The adsorption conformed to Langmuir adsorption isotherm and followed pseudo first order kinetics. The strong magnetic nature of the adsorbent facilitated easy separation and recycling after adsorption. The present work provides insights into the use of aggressive weeds for the phytogenic development of eco-compatible adsorbents for rapid chromium reduction and removal.

1. Introduction

Chromium exists in its trivalent and hexavalent state in nature. Cr (III) is considered an essential human dietary element whereas Cr(VI) is highly toxic and acts as carcinogens, mutagens, and teratogens in biological systems. It is well established that the toxicity of Cr(VI), is higher than that of Cr(III), due to the increased solubility of Cr(VI) species compared to Cr(III), and easy absorption and accumulation in kidneys, stomach, and liver [1]. Extensive use of hexavalent chromium in various industries including electroplating, leather tanning, metal fabrication, and finishing has exacerbated Cr(VI) contamination in water bodies [2]. Existing literature indicates the presence of unacceptable quantities of Cr(VI) in drinking water, soil, and plants [3–6] which demands immediate and effective remediation strategies.

Assorted techniques such as membrane filtration, ion exchange, reverse osmosis, electrochemical treatment, solvent extraction, photocatalysis and adsorption/biosorption have been developed for the removal of chromium from industrial sewage. Researchers have fabricated various materials including surface engineered metal oxide nanosystems and polymer nanocomposites for efficient removal of chromium [6–10]. Among these, adsorptive techniques play pivotal role owing to their effortless execution, appreciable efficiency, and economic viability [11,12]. Numerous reports on strategic development of adsorbent systems including modified GO [13,14] supports the efficacy of the technique. Different forms of iron oxides and hydroxides are reported as efficient adsorbents for heavy metal ions from water [15–17] and various physical, chemical and biological methods have been reported for the synthesis of iron oxide nanoparticles (IONPs) as well [18]. Additionally, the magnetic properties of IONPs facilitate easy separation of the exhausted adsorbents, making IONPs more desirable. Recently tailor-made IONPs were synthesized via co-precipitation, hydrothermal and sol-gel techniques coupled with the aid of constrained environments or molecular cages (e. g., microemulsions, micelles, dendrimers, cyclodextrins) [19], acoustic cavitation [20] and microwave irradiation [21]. Iron oxides are also extensively used to magnetize carbonaceous adsorbent systems [22,23]. However, most of these methods use separate stabilizing and templating agents to attain precise control over the nanoparticle size and morphology, as well as to prevention of

* Corresponding author at: University of Calicut, Department of chemistry, calicut university P O, CALICUT, Kerala 673 635, India.
E-mail address: drabrahamj@gmail.com (A. Joseph).

https://doi.org/10.1016/j.materresbull.2022.112130
Received 29 June 2022; Received in revised form 8 November 2022; Accepted 17 December 2022
Available online 17 December 2022

aggregation of the nanoparticles [24] which results in expensive and laborious work.

Possibilities of using biogenic resources for the removal of heavy metals has recently gained global attention [25,26]. Phytogenic synthesis of IONPs provides a sustainable and facile one-pot alternative for the fabrication of surface-modified IONPs. Plant extract-mediated synthesis of IONPs offers strategic synthesis of different iron oxide nanoparticles such as goethite, hematite, maghemite and magnetite [27–29]. Magnetite nanoparticles are frequently opted for water remediation over other IONPs owing to their low toxicity, ease of functionalization and easy separation ability. There are reports on successful fabrication of hierarchical nanostructures from various leaf extracts [30–34] for the removal of Cr(VI).

Chromolaena odorata is an aggressive, allelopathic tropical weed that is listed in 100 of the world's worst invasive alien species by IUCN. They cause severe disturbances in the eco-diversity and economy during their invasive propagation. *C. odorata* grows in dense pure stands and blooms enormously during the summer. The blooms produce around 93,000-160,000 light, hairy seeds/plants, which contribute to the invasive nature of the species [35]. They cause extensive and irreversible impacts on the native biodiversity and landscapes, therefore should be strictly controlled. Since the plant covers large areas of land, around the globe, manual removal would be impractical. Hence the most sustainable alternative is to identify the possible applications of the plant and monetize them.

In this study, we report for the first time, an environmentally benign synthesis route for superparamagnetic iron oxide nanoparticles employing *Chromolaena odorata (L) King & Robins* flower extract (COFE). The work explores the simultaneous use of COFE as a reductant and capping agent in the synthesis of magnetite nanoparticles. The study was further extended for the removal of Cr(VI) from contaminated water utilizing *Chromolaena odorata*-derived iron oxide nanoparticles(CMNs) with a special concern towards reducing the contact time required for removal of the pollutant substantially. The work addresses two major environmental concerns, alien invasive species and heavy metal pollution in a sustainable approach by engineering biocompatible and recyclable CMNs using the former. The results of the study are promising compared to existing reports elsewhere.

2. Materials and methods

2.1. Materials

$FeCl_3.6H_2O$, $NaHCO_3$, $K_2Cr_2O_7$and $C_{13}H_{14}N_4O$ were purchased from Merck and used without further purification. *Chromolaena odorata* flowers were collected locally from in and around the University of Calicut, Kerala. An herbarium sample was prepared and deposited (Fig. S1) in Calicut University Herbarium (CALI), University of Calicut (voucher no.7086) for future references. Fresh, healthy flowers were cleansed thoroughly with tap water and air-dried before extraction of the phytochemicals.

2.2. Synthesis of magnetite nanoparticles

Initially, 20g of desiccated flowers were added into 350ml of distilled water and then stirred magnetically for 3 hours to obtain *Chromolaena odorata* flower extract (COFE)at 80°C. The temperature of the system was maintained at 40°C overnight for effective leaching of phytochemicals into the solvent. The cooled crude mixture was then strained through a muslin cloth to obtain COFE. Qualitative phyto-screening [36] of COFE was conducted and total phenolic [37] and flavonoid content was estimated using standard testing methods [38]. To 50 ml of the COFE, 30 ml of 0.032 M $FeCl_3$ solution was introduced under vigorous magnetic stirring followed by gradual addition of 0.52g of $NaHCO_3$. The resultant black solution was ultrasonicated for 15 minutes by Branson 150 D Sonifier with an immersed ultrasonic horn (2.38mm, 25 kHz) and was followed by magnetic stirring for 1 hour at room temperature. The mixture was then transferred into a 100ml Teflon-lined autoclave and was kept in a hydrothermal oven at 180°C for different periods (8, 12, and 24 hours). The black, lustrous product formed was magnetically collected, sequentially leached with ethanol and water, and dried at 70°C to obtain CMNs. The synthesized products were labelled as CMN-8, CMN-12, and CMN-24.

2.3. Characterization of CMNs

The crystal structure and phase purity of CMNs were identified by powder X-ray diffraction analysis (XRD) on a Malvern-PanAnalytical X-ray diffractometer. The crystallite size of the CMNs was calculated from the XRD pattern using the Scherrer equation. Fourier transform infrared spectroscopy measurements were done using JASCO FTIR- 4600 spectrophotometer. The morphology of CMNs was observed using Carl-Zeiss (Sigma) field emission scanning electron microscopy and Jeol/JEM 2100 high-resolution transmission electron microscope. The magnetic properties were investigated using Lakeshore VSM 7410 vibrating sample magnetometer at 298 K. Zeta potential measurements of CMNs were conducted on Brookhaven PALS zeta potential analyzer Ver.5.60. Energy dispersive X-ray (EDAX) composition analysis (Bruker Nano X-Flash Detector) and Brunauer-Emmett-Teller (BET) analysis (Belsorp) and X-ray photoelectron spectroscopy (Omicron Nanotechnology) was used for an in-depth analysis of the surface composition, valence state and mechanism of Cr (VI) removal by CMNs.

2.4. Adsorption batch studies

A stock solution of $K_2Cr_2O_7$ (500 mgL^{-1}) was prepared and simulated effluents were prepared by diluting the stock solution with deionized water as required. Adsorption batch studies were conducted in glass vessels kept on a platform shaker. The adsorption experiments were performed by dispersing CMNs (2g L^{-1}) into 20 ml of Cr(VI) solution (100mg L^{-1}). CMNs were separated using an external magnet and the supernatant solution was retrieved at regular contact intervals. The procured analyte was evaluated under JascoV-770 UV-Vis-NIR spectrophotometer, using 1,5 diphenyl carbazide as a complexation agent at 543nm to estimate the residual Cr(VI) [39]. The total residual chromium content was detected using ICPMS to estimate the quantity of Cr(III) in the adsorbate solution [13]. The contact time and dosage of CMNs were optimized to identify the most suitable adsorbent for Cr(VI) removal. The effect of pH, temperature, and initial concentration of Cr(VI) on the adsorption capacity of selected CMN were also investigated. The effect of pH was investigated in a range of pH 2-8. Cr(VI) solutions ranging from 10 mgL^{-1} to 500 mg L^{-1} were investigated to evaluate the effect of initial pollutant concentration on adsorption capacity. The effect of temperature on adsorption efficiency was analyzed in the temperature range of 30-60°C. The experiments were carried out in triplicates and the mean values were considered.

3. Results and discussion

The XRD analysis confirmed the formation of pure magnetite nanoparticles, after hydrothermal treatment for 8 hours. Fig. 1a depicts XRD patterns of the CMNs before hydrothermal treatment and CMN-8. CMNs are unable to form without hydrothermal treatment. All of the diffraction patterns of CMN-8 match well with the normal diffraction patterns of inverse spinel Fe_3O_4 and can be indexed to PDF no. 19–0629 [40]. Further increase in the reaction time resulted in intense peaks in the XRD pattern, indicating an increase in the crystallinity of the CMNs (Fig. S2). The broadening of the peaks results in high FWHM values indicating the small size of the formed CMNs crystallites. Crystallite size was calculated using Scherrer's equation on the (311) plane and was found to be ~7nm, 8nm, and 9 nm for CMN-8, CMN-12, and CMN-24 respectively. The increase in crystallite size with an increase in the reaction time is due to

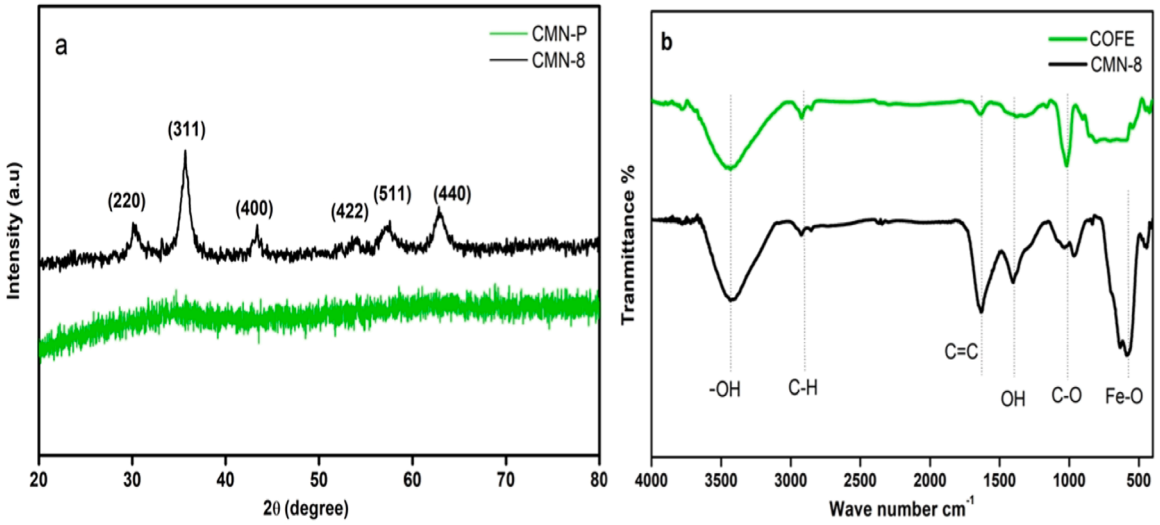

Fig. 1. a) XRD pattern of sample prior to hydrothermal treatment (CMN-P) and CMN-8 b) FTIR spectra of COFE and CMN-8.

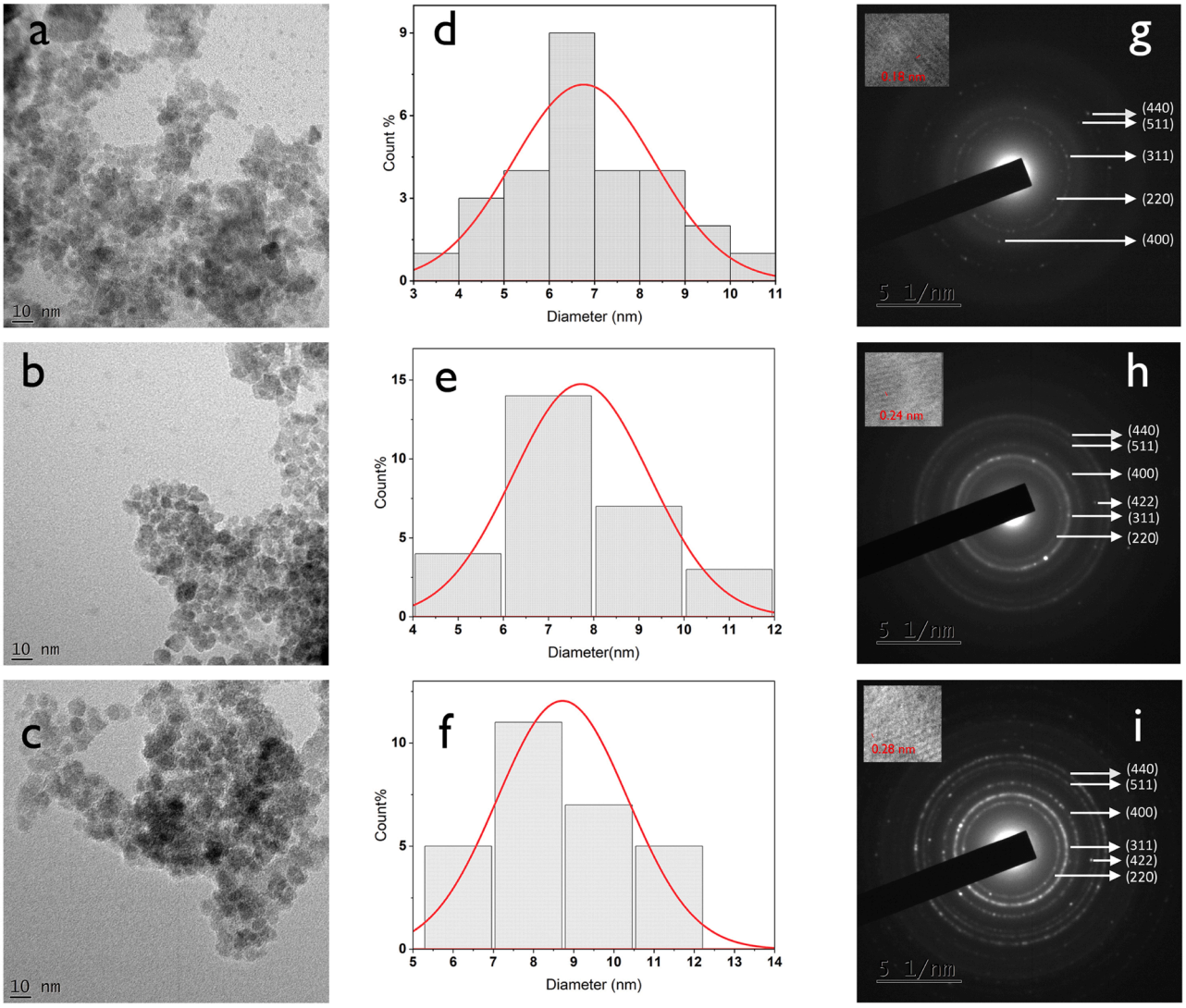

Fig. 2. HRTEM images of a) CMN-8, b) CMN-12, c) CMN-24; particle size distribution analysis of d) CMN-8, e) CMN-12, f) CMN-24; SAED patterns of g) CMN-8, h) CMN-12, i) CMN-24 (insets showing the interplanar distance).

the enhanced grain growth during prolonged treatment [41]. FTIR spectra of COFE and CMN-8 are illustrated in Fig. 1b. The peaks around 3435 cm^{-1} and 1378 cm^{-1} in COFE are attributed to OH stretching and bending vibrations. The peak at 2927 cm^{-1} was assigned to C-H stretching vibration and the peak appeared around 1629cm^{-1} was assigned to aromatic C=C stretching vibrations from polyphenols, while the peak at 1058cm^{-1}corresponds to C-O bending vibrations of the biomolecules [42].The reoccurrence of the aforementioned peaks along with a distinct peak at 575 cm^{-1}corresponding to metal-oxygen stretching vibrations (Fe–O) at the tetrahedral site [43] verifies the formation of magnetite conjugated with phytochemical fragments derived from the COFE.

The HR-TEM micrograph (Fig. 2a) exhibits nearly spherical and monodisperse particles with minimal aggregation. This substantiates the effective surface refinement achieved through ultrasonic assistance and the reduced magnetic dipolar interaction between particles. The estimated average particle diameter for CMN-8 using the size distribution analysis was approximately 6.75±1.56 which is comparable with the XRD results. Thus, it can be inferred that phytochemicals exist as a thin layer anchored on to the magnetite surface. The increase in reaction time resulted in distinct changes in morphology. The increased polydispersity and particle agglomeration with the increase in reaction time is evident from the TEM micrographs (Fig. 2b, 2c, Fig. S3). Particle size distribution plots (Fig. 2d-f) indicated slight increase in the particle size in the order CMN-8<CMN-12<CMN-24. The interplanar spacing of approximately 1.8Å observed for CMN-8 concurs well with the lattice spacing of the (511) planes in crystalline Fe_3O_4. Moreover, the selected area electron diffraction (SAED)pattern of the CMN-8 (Fig. 2g) in the selected area exhibits five distinguishable crystal planes of (440), (511), (400), (311), and (220) which is in agreement with XRD results [44]. The SAED pattern shows that the prepared sample is polycrystalline with a cubic inverse spinel crystal structure. The SAED pattern of CMN-12 and CMN-24 revealed six distinguishable crystal planes as presented in Fig. 2h and 2i.

Low temperature N_2 adsorption-desorption isotherms were obtained to determine the surface area and nature of the porosity of CMN-8. Though the result (Fig. 3) resembles type-IV isotherm, the absence of plateau region in the higher-pressure region categorizes it as a pseudo-type II isotherm. The presence of hysteresis loop at p/p_0 =0.6-0.9 indicates a typical H3 type hysteresis indicating the presence of grooves created by non-rigid aggregated particles [45]. The pore distribution analysis by Barrett-Joyner-Halenda's (BJH) method revealed multiple peaks indicating the presence of pores of different types. The peaks represent the interstices created by the boundaries of the nanoparticles. The specific surface area and the mean pore diameter obtained for CMN-8 calculated were 8.12 m^2g^{-1} and 28.2nm respectively. The average pore volume calculated was 0.05 cm^3g^{-1} indicating the low porosity of the material.

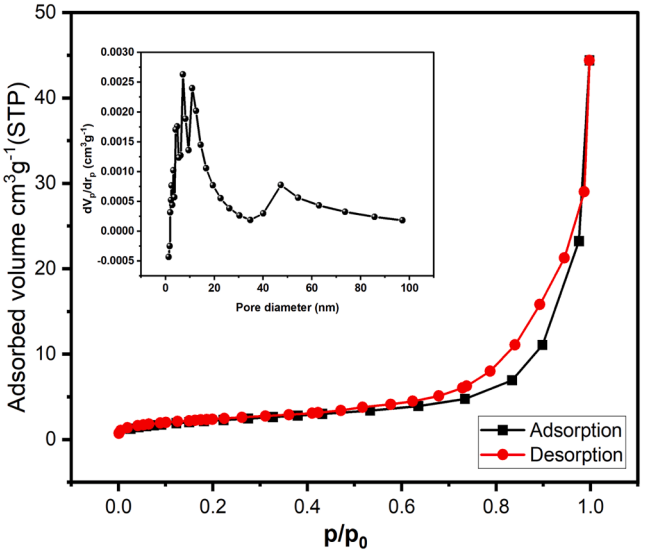

Fig. 3. N_2 adsorption-desorption isotherm of CMN-8; inset displaying the BJH plot.

3.1. Mechanism of CMN formation

The aqueous extracts of aerial parts of the *Chromolena odorata* are reported to contain an appreciable number of polyphenols and flavonoids in addition to other hydrophilic biomolecules like saponins. These phytochemicals provide a variety of iron-binding sites such as 6,7- dihydroxy moieties, B-ring catechol, and 2,3 double bonds [46]. Primary phytoscreening of COFE used in this work revealed the presence of saponins, tannins, polyphenols, flavonoids, alkaloids, and glycosides in the aqueous extract. The total phenolic content and total flavonoid content estimated were 175.69±1.21 mg GAE/g and 24.72±0.87 (mg QE/g) respectively. The instantaneous change in the brown colour of COFE to dirty green upon the addition of $FeCl_3$ indicates the complexation of Fe^{3+} ions with polyphenols/flavonoids [47]. The addition of $NaHCO_3$ neutralizes HCl formed in the reaction medium enabling COFE to reduce Fe^{3+} ions. Ultrasonic homogenization of the colloidal solution resulted in the formation of less aggregated CMN with significant yield. It can be speculated that $NaHCO_3$ acts as heterogeneous nucleating centers during the hydrothermal treatment. The evolution of CO_2 suggests a plausible gas template mechanism of nucleation [48]. The local temperature gradient formed on the surface of the nanoparticles accelerates hydroxide to oxide conversion. The presence of hydrophilic phytochemicals in the reaction medium has a significant role in decreasing the frequency of collisions between the newly formed nanoparticles. As the collisions decrease, the oriented attachment and Ostwald ripening rate diminish, resulting in smaller crystallite size. Self-capping of phytochemical fragments controls the aggregation of nanoparticles and provides CMNs appreciable wettability, which in turn facilitates its use in water remediation.

3.2. Adsorption studies

The effect of contact time with constant dosage on adsorptive removal of Cr(VI) by CMNs is depicted in Fig. 4a. The estimated optimum contact time to enable 99.28% removal of Cr(VI) ions from the system is 10 minutes for CMN-8. The equilibrium adsorption capacity (q_e)was calculated as

$$q_e = \frac{(C_0 - C_e)v}{m} \quad (1)$$

where C_0 and C_e are the initial and equilibrium concentration of Cr(VI) ions respectively. Here v is the volume of pollutant considered and m denoted the mass of the adsorbent taken. The maximum adsorption capacity reached 49.6 mg g^{-1} in 10 minutes. The change in adsorption capacity inflicted upon a further increase in the contact time was negligible. Compared to various existing reports, the performance time for CMN- 8 to achieve 99.28% removal of 100 mg L^{-1} of Cr(VI) solution is significantly lower [49,50]. The Cr(III) content in the adsorbed solution was 0.19 ppm, indicating that only a small fraction of the reduced chromium species is released back to the solution by CMN-8. The adsorption capacity of CMN-12 and CMN-24 were recorded as 36.5 and 23.5 mg g^{-1} respectively (Fig. 4a). The decrease in adsorption capacity is associated with the reduction in the active surface area affected by the increased particle size and agglomeration. The increased hydrothermal reaction period may have triggered the degradation of phytoconjugates on the surface of nanoparticles leading to fewer active sites for adsorption. Therefore CMN-8 was chosen as the suitable sample for the follow-up experiments to further explore the physicochemical and

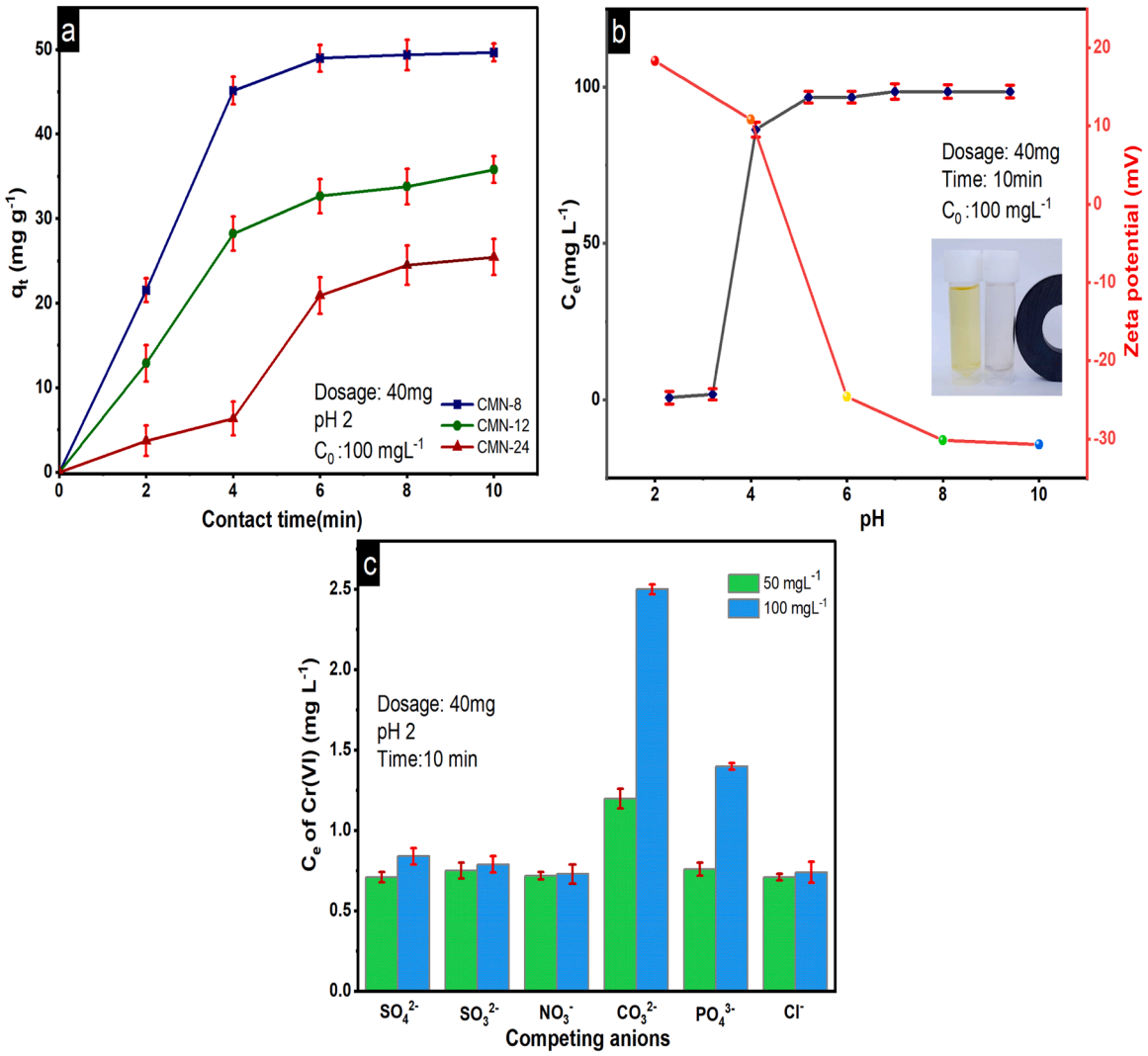

Fig. 4. a) Adsorption capacities of CMNs prepared at different reaction periods, b) Effect of pH on zeta potential of CMN-8 and Cr(VI) removal efficiency; inset showing 100 mgL^{-1} Cr(VI) solution before and after adsorption by CMN-8 c) Effect of different concentrations of coexisting anions on adsorption efficiency of CMN-8.

adsorption properties of CMN towards Cr(VI) species in aqueous effluents.

3.3. 1. Effect of pH and interfering ions

The efficiency of Cr(VI) removal depends crucially on the pH of the solution. The speciation of Cr(VI) in an aqueous solution varies with pH. $HCrO_4^-$ predominates when pH is below 4, however, as the pH increases CrO_4^{2-} dominates in the solution. The lower adsorption free energy of $HCrO_4^-$compared to CrO_4^{2-}make it more susceptible to adsorption [51]. A prominent increase in the adsorption capacity of CMN-8 with a decrease in the pH is evident in Fig. 4b. Maximum adsorption efficiency of CMN-8 was observed at pH 2-4. The plot of zeta potential against pH depicted in Fig. 4b indicated that at lower pH the CMN-8 surface is sufficiently protonated yielding electrostatic attraction towards $HCrO_4^-$. Whereas, an increase in pH generates a more negative charge on the surface of CMN-8 initiating electrostatic repulsion between Cr(VI) species and the adsorbent, thus reducing the Cr(VI) adsorption onto CMN-8.

Cr(VI) in effluents often coexist with other anions such as chlorides, nitrates, sulfates and carbonates. The potential of CMN-8 in presence of interfering anions was investigated with different concentrations of different anions. The experiments testified that CMN-8 is a potent adsorbent against Cr(VI) even at higher concentrations of various anions (Fig. 4c). However, adsorption capacity deteriorated evidently in presence of carbonate and at a high concentration of phosphate ions. These ions can compete with $HCrO_4^-$ ions for active sites on the adsorbent. Moreover, the higher affinity of these anions towards iron may decelerate the adsorption of Cr(VI) by blocking the reactive sites. Fig. 5 illustrates a schematic representation of synthesis and adsorptive removal of Cr(VI) by CMN-8. A list of selected recent reports on biogenic iron oxide -Cr(VI) adsorbent systems is presented in Table 1 [52–57]

3.4. Adsorption isotherms

Batch equilibrium adsorption experiments were used for adsorption assessment by simulating plots (Fig. 6a) of both Langmuir and Freundlich adsorption models. According to Langmuir model, for homogenous systems,

$$q_e = \frac{q_m b C_e}{1 + bC_e} \quad (2)$$

where q_e is the amount of Cr(VI) adsorbed at equilibrium, q_m is the maximum amount of Cr(VI) adsorbed per unit weight of the adsorbent (mg g^{-1}) and b is the Langmuir adsorption isotherm constant. The Freundlich model can account for multilayer and non-equivalent adsorption sites. According to the Freundlich adsorption model

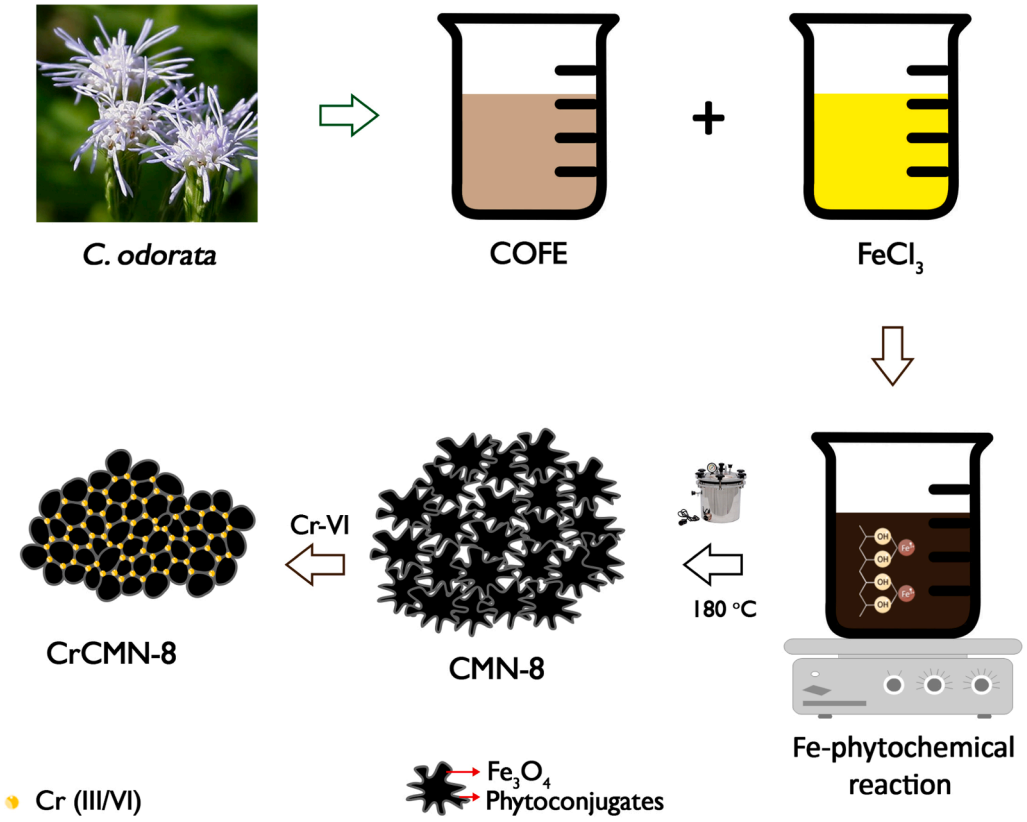

Fig. 5. Schematic illustration of synthesis and adsorption of Cr(VI) on CMN-8.

Table 1
List of recent reports of iron oxide-based adsorbents for chromium removal.

Adsorbent	Synthesis route of iron oxide	Adsorbent dosage	Initial Cr(VI) concentration	pH	Optimum contact period	Adsorbent Capacity/Removal percentage	Reference
Bimetallic GT nZVI/Cu	Green tea mediated	0.4 gL^{-1}	5 mgL^{-1}	5	60	94.7%	[52]
Siderite/magnetite	Microbial synthesis	1 gL^{-1}	50mg L^{-1}	4	120	9.9%	[53]
Magnetite NPs	Fungal extracellular synthesis	2.5 gL^{-1}	50mg L^{-1}	3	120	99.75%	[54]
Biochar-iron oxide composite	Chemical method	2 gL^{-1}	40 mg L^{-1}	4.7	160	24.37 mg g^{-1}	[55]
PPy - Fe_3O_4– Seaweed composite	Chemical method	0.1 gL^{-1}	50 mg L^{-1}	2	30	96.36%	[56]
Biochar iron oxide composite	Chemical method	0.5 gL^{-1}	30 mg L^{-1}	5	400	48.1 mg g^{-1}	[57]
CMN-8	**Phytogenic synthesis**	**0.2 gL^{-1}**	**100 mg L^{-1}**	**2**	**10**	**99.28%**	**Present work**

$$q_e = K_F C_e^{1/n} \quad (3)$$

Where K_F and n are Freundlich adsorption isotherm constants and n is the measure of the heterogeneity of the system.

Table 2 indicated that the Langmuir model effectively describes the adsorption of Cr(VI) onto CMN-8 as dominantly monolayer adsorption. The maximum adsorption capacity(q_m) for CMN-8 towards Cr(VI) was 173.12 mg g^{-1}, which corresponds to the complete monolayer coverage on the CMN-8 surface. The affinity between the adsorbent and adsorbate is quantified by evaluating the dimensionless separation factor R_L which is given by the equation

$$R_L = \frac{1}{1 + bC_0} \quad (4)$$

where C_0 is the highest initial adsorbate concentration. For favorable adsorption $0 < R_L < 1$ and for unfavorable adsorption $R_L > 1$ or $R_L = 1$.

The R_L value obtained for adsorption of Cr(VI) on CMN-8 was 0.0097. From the obtained R_L value, a favorable parameter K_{C0} can be derived.

$$K_{C_0} = \frac{1}{R_L} - 1 \quad (5)$$

The adsorption is considered favorable when the K_{C0} value is between 1 and 10. K_{C0} values higher than 10 denote spontaneous and highly probable adsorption. The derived value of K_{C0} for CMN-8 is 525.32 and it indicated the highly favorable nature of its adsorption.

3.5. Kinetics of adsorption

The rate of adsorption of Cr(VI) by CMN-8 can be determined by employing different kinetic models. Here we have considered pseudo-first order, pseudo-second order, and Elovich models for kinetic studies as depicted in Fig. 6b.The model which fits best for the experimental data were identified from the regression correlation coefficient

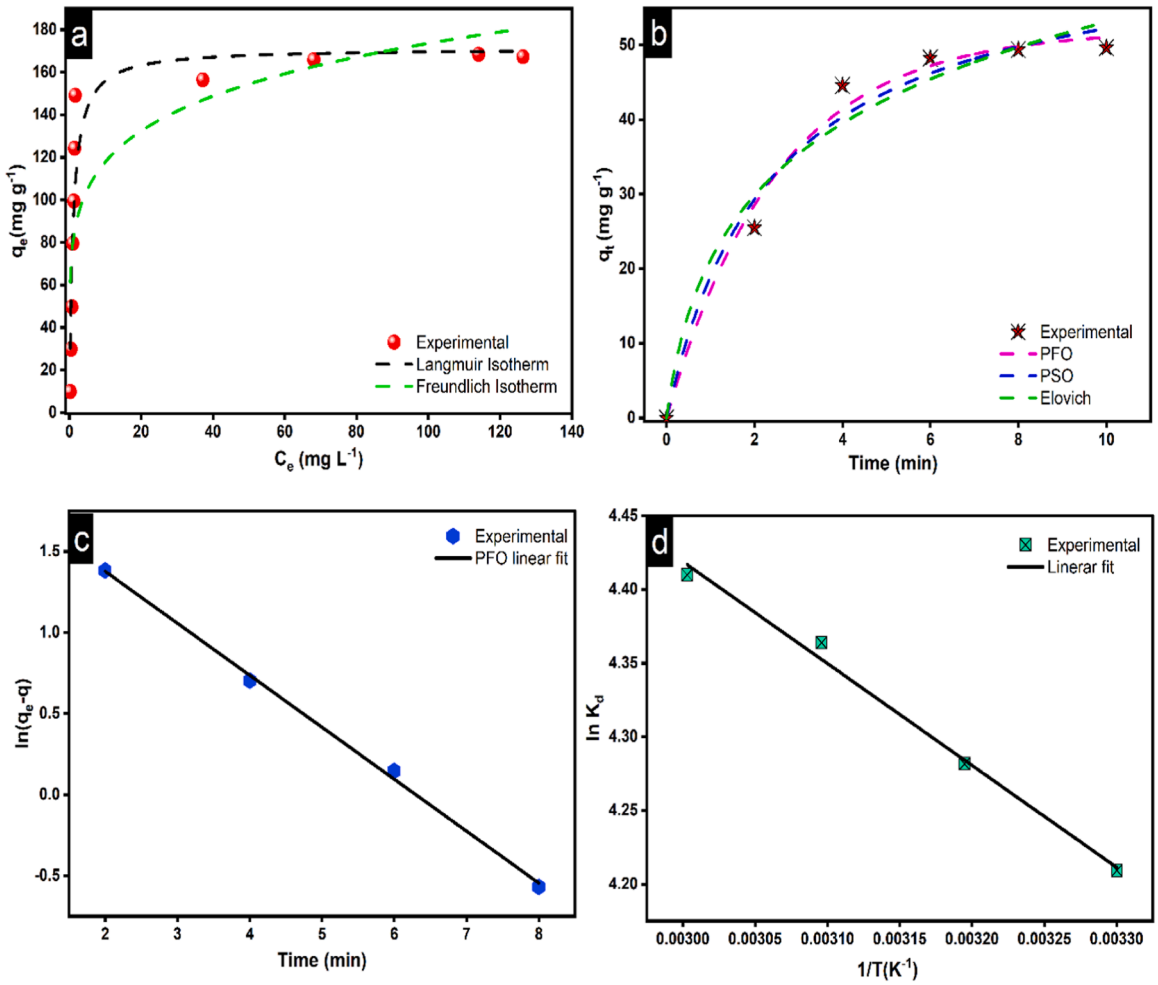

Fig. 6. a) Nonlinear adsorption isotherm fit for Cr(VI) adsorption on CMN-8, b) Nonlinear fit of different kinetic models for Cr(VI) adsorption on CMN-8 c) linear fit of pseudo first order reaction d) thermodynamic study for Cr(VI) adsorption on CMN-8.

Table 2
Parameters obtained from adsorption isotherm and kinetic modeling studies on adsorption of Cr(VI) by CMN-8.

Models		Parameters		R^2
Isotherms	Langmuir	q_m(mg g^{-1}) =173.12	K_L =1.02	0.9245
	Freundlich	K_F =79.98	n =3.5	0.6834
Kinetics	Pseudo first order	q_e(mg g^{-1}) =51.98	k_1(h^{-1}) =0.397	0.9886
	Pseudo second order	q_e(mg g^{-1}) =64.92	k_2(g (mg h)$^{-1}$) =0.0063	0.9783
	Elovich	a(mg g^{-1}) =44.72	b =0.063	0.9675

(R^2) values. From the linear regression analysis, it was observed that the experimental results correlated well with pseudo-first order adsorption (Fig. 6c). Table 2 summarizes the data for kinetic studies and adsorption isotherm studies of Cr(VI) adsorption on CMN-8 simulated with different theoretical models.

3.6. Thermodynamics of adsorption

The effect of temperature on the adsorption process was investigated by conducting adsorption experiments at different temperatures. In this work, the batch thermodynamic experiments were studied between 303 and 333 K, and the following equations were applied to compute the thermodynamic parameters for the adsorption of Cr(VI) ions.

$$K_d = \frac{q_e}{C_e} \tag{6}$$

$$lnK_d = \frac{-\Delta H}{RT} + \frac{\Delta S}{R} \tag{7}$$

$$\Delta G = \Delta H - T\Delta S \tag{8}$$

where K_d represents the equilibrium constant. Fig. 6d shows the simulated plot of ln K_d against 1/T for adsorption of Cr(VI) ions on CMN-8 at different temperatures. Table 3 summarizes the obtained thermodynamic parameters. The positive ΔH value indicated the endothermic nature of the adsorption. The positive ΔS values suggested the rising disorder at the interface during the adsorption of Cr(VI) ions onto CMN-8. The high negative values of ΔG indicated the spontaneity of the process.

Table 3
Thermodynamic parameters of adsorption of Cr(VI) onto CMN-8.

Temperature (K)	ΔG (kJmol^{-1} K^{-1})	ΔH(kJ mol^{-1} K^{-1})	ΔS (Jmol^{-1} K^{-1})
303	-10.608	5.744	53.97
313	-11.148		
323	-11.687		
333	-12.227		

3.7. Mechanism of adsorption

FTIR studies revealed the presence of phyto-conjugates and surface hydroxyls on CMN-8. At lower pH, the terminal hydroxyl groups derived from COFE get protonated inversing the inherent negative charge on the surface. The positive charge prevailing on the CMN-8 up to pH 4.8 enables electrostatic attraction towards $HCrO_4^-$ species initiating the adsorption process. Fig. 7 illustrates the XPS profile of CMN-8 before and after adsorption of chromium. XPS confirms the formation of pure magnetite with phyto-conjugate stabilization with surface elemental composition of Fe(9.15%), O(40.57%) and C(50.28%). The comparatively low amount of iron indicates the efficient capping of the magnetite core by the phytochemical fragments. The Fe 2p core-level spectrum of CMN-8 has two peaks at ~710.8eV and ~724.1eV verifying the magnetite phase. The fitted Fe 2p spectrum (Fig. 7a) consists of peaks at 710.1, 711.3, 713.1, 723.4, 724.1 and 725.3 eV. The peaks at 710.1and 723.4 eV correspond to the presence of Fe^{2+} species in the octahedral (O_h) site. Fe^{3+} species in the octahedral sites are found at a binding energy of 711.3 and 724.1 eV. The peaks at 713.1 and 725.3eV are attributed to Fe^{3+} in tetrahedral sites (T_d). A weak shoulder displayed at ~719.2 eV corresponds to vacancy cascade(VC) commonly observed in iron oxide species [58]. A slight chemical shift to the higher binding energy from that of pure magnetite can be attributed to the phyto-conjugation on the surface of CMN-8. The O 1s score-level spectrum (Fig. 7b) exhibits peaks at ~529.4eV and 530.6eV correlated to Fe-O and C-O moieties. The peak with higher binding energy at 531.9 eV is attributed to surface hydroxyl groups adhered to CMN-8 [57]. The C 1s profile of CMN-8 (Fig. 7c) was fitted into four peaks with binding energies ~285, 286.5, 289.3, and 292.3eV corresponding to C-C, C-O, C=O moieties, and π-π interactions respectively[59]. However, upon adsorption of chromium, the peak at ~292.3eV disappeared whereas the peak at 289.3eV displayed a chemical shift to 288.5eV. There was a concomitant increase in the percentage composition of C-C and C-O bonds and a decrease in C=O bonds. O 1s spectra also displayed evident post adsorption changes. Dissolution of the peak at 531.9eV indicated active participation of surface hydroxyl groups in adsorption of Cr(VI). The prominent increase in percentage composition of the peak corresponding to the Fe-O (metal–O) bond (529.4eV) assisted with peak shift to higher binding energy (529.8eV) confirms the deposition of chromium to CMN surface through Cr-O bonds. Fe 2p spectrum exhibited a chemical shift to lower binding energies and the weak shoulder at ~719.2eV disappeared possibly due to the association of O-Cr on the CMN-8 surface. Cr 2p core-level spectra(Fig. 7d) displayed peaks at 576.6eV and 578.2 eV corresponding to Cr(III) and Cr(VI) respectively

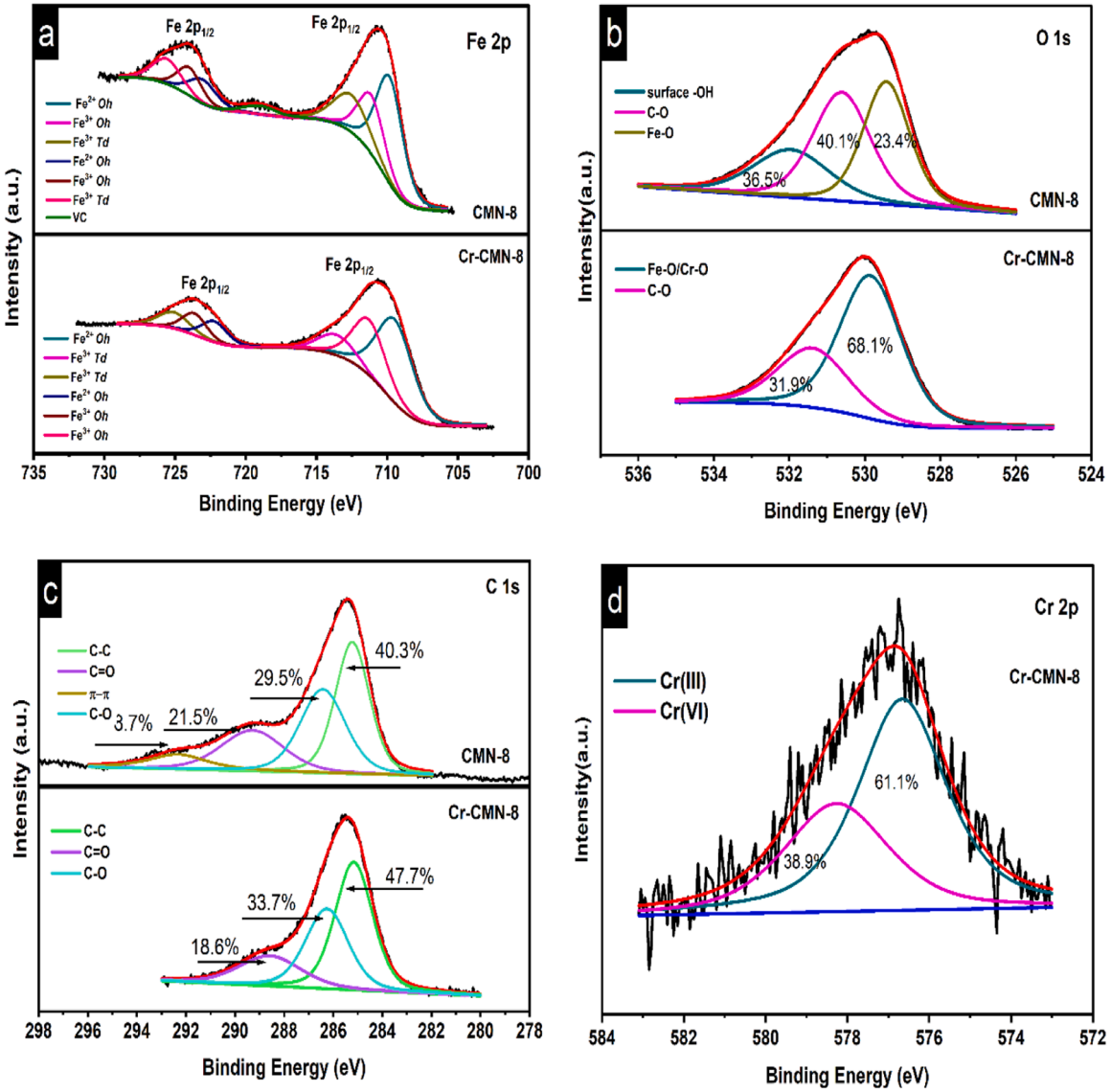

Fig. 7. Pre and post adsorption XPS profile of CMN-8 for a) Fe 2p b) O 1s c) C 1s and d) Cr 2p core levels.

evincing the reduction of toxic hexavalent chromium on the CMN-8 surface [57]. The surface element composition after adsorption was calculated as (Fe-8.76%, O-45.79%, C-43.61%, and Cr-1.84%). The increase in the percentage of oxygen after adsorption indicates the association of oxygenated chromium species on the surface. The comparably evident reduction in the amount of carbon shows that the adsorbate species are linked to the phytochemical fragments capping the magnetite core rather than directly to the Fe atoms.

Scanning electron microscopy equipped with energy dispersive spectroscopy (FESEM-EDX) was used to investigate morphological and compositional changes in CMN-8 post adsorption. The FESEM images (Fig. 8a, 8b) of CMN-8 illustrate unique morphology of an assembly of tiny nanobuds resembling a 'broccoli head'. There are numerous void interstices surrounding each cluster of nanobuds as predicted by the N_2 sorption analysis. These interstices act as interlinking channels that facilitate the easy transport and anchoring of Cr(VI) species on the adsorbent surface. Up on adsorption of Cr(VI), surface morphology of CMN-8 changed evidently. More protruding clusters appeared on the surface and the void interstices were filled with deposition of chromium species (Fig. 8c,8d). Images of elemental investigation on exhausted adsorbents are displayed in Fig. 9a-9f. EDAX spectra of CMN-8 revealed the presence of Fe (21.34%), O (24.75%), and C (53.91%), and confirming the phytoconjugation on the iron oxide surface (Fig. 9g). Whereas EDAX analysis of Cr-CMN-8 (Fig. 9f) displayed the presence of Cr and negligible changes in the composition of other elements (Fe-20.25%, O-30.23%, C-47.39% and Cr-2.13%).

The change in magnetic properties of magnetic adsorbents after adsorption is rarely investigated. Magnetic properties of CMN-8 before and after adsorption (Fig. 10) differed prominently. Owing to the smaller size of particles CMN-8 exhibited superparamagnetic nature with a saturation magnetization (M_s) of 38.4 $emug^{-1}$. The lower saturation magnetization value originated from the small size of CMN-8 and the nonmagnetic phytochemical capping derived from COFE. M_s after adsorption of Cr(VI) increased up to 52.17 $emug^{-1}$. A similar rise in saturation magnetization is reported for iron oxide nanoparticles upon doping with chromium [60] owing to the inherent paramagnetic nature and high magnetic moment of chromium. Ferromagnetic nature post adsorption originated from the obvious increase in the size of particles due to bulk chromium association. The remarkable change in the hysteresis upon adsorption further substantiates the deposition of chromium on the CMN-8 surface. XRD studies on CMN-8 post adsorption lacked any characteristic peaks of chromium refuting any changes in the crystal structure.

The plausible pathway of Cr(VI) removal by CMN-8 proceeds through 1) In acidic environment electrostatic attraction of chromate anions on to CMN-8 surface, 2) The unique surface morphology of CMN-8 traps the Cr(VI) species exposing it to reduction by the nearby electron donor groups, 3) The morphology of CMN-8 prevents the release of the reduced Cr(III) and adsorbed Cr(VI) species. The minute amount of Cr (III) in the adsorbed solution indicate that the reduced chromium species is also anionic in nature and is effectively sequestered by CMN-8. Since the XRD profile of CMN-8 did not alter after adsorption it is reasonable to speculate that there might be an amorphous layer of chromium post-adsorption which lead to the higher saturation magnetization moment. FESEM images of exhausted adsorbents also support extensive deposition of chromium species on the surface. A schematic representation of

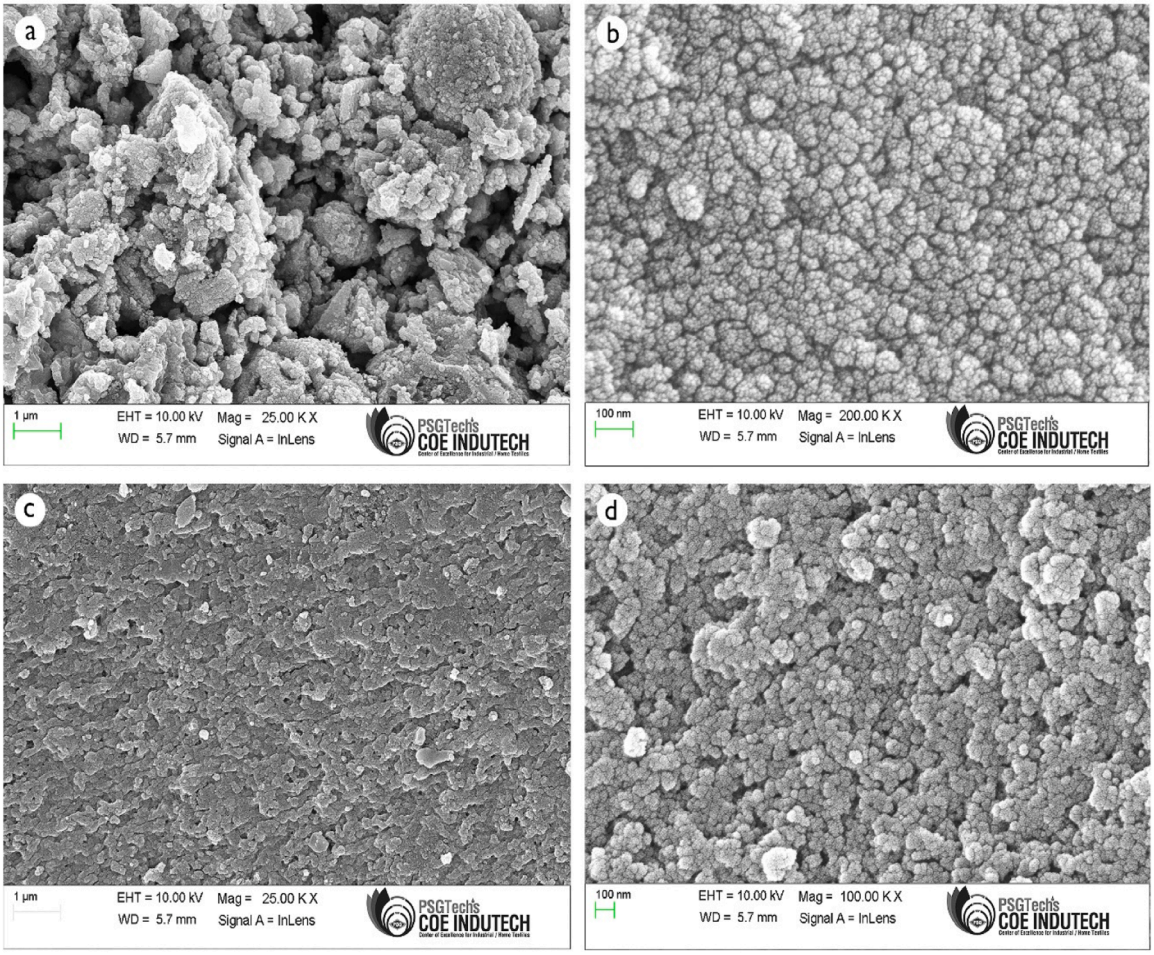

Fig. 8. FESEM images of a,b)CMN-8, c,d) Cr-CMN-8.

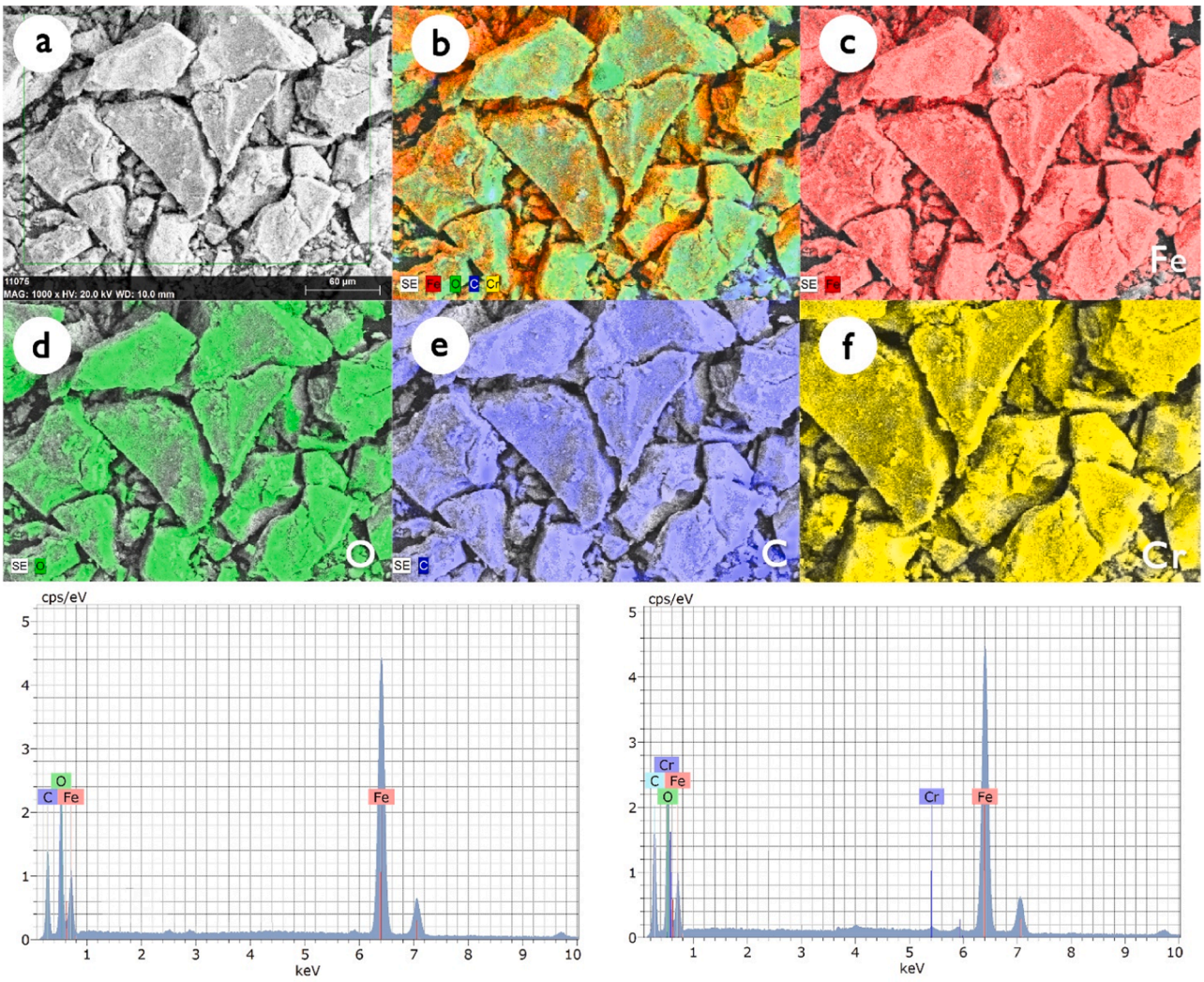

Fig. 9. a-f) Elemental mapping profile of Cr-CMN-8, EDAX profile of g) CMN-8, h) Cr-CMN-8.

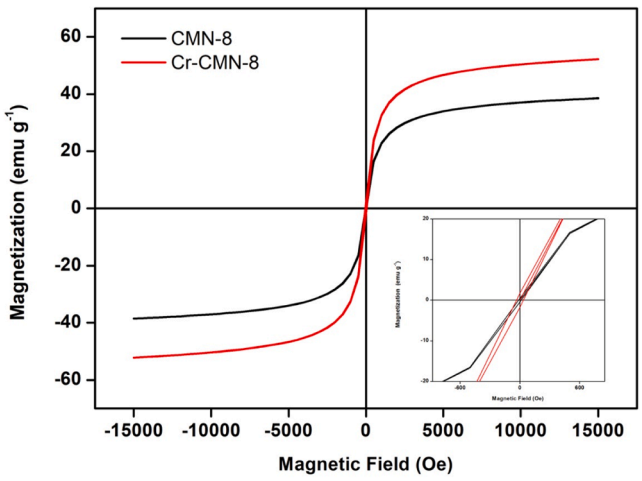

Fig. 10. M-H plot of CMN-8 pre and post-adsorption of Cr (VI); inset showing close up image of the center of the plot.

the mechanism is illustrated in Fig. 11. The decrease in adsorption capacity with increase in duration of hydrothermal treatment can be correlated to the decrease in the phytoconjugates content evident from the XRD results (Fig. S3). The increase in crystallinity of the sample suggests lower phytoconjugation in CMN-12 and CMN-24, which along with increased agglomeration reduce the efficiency of adsorption.

3.8. Recyclability

The magnetic property of the adsorbent made recovery and regeneration of the exhausted adsorbent easy and fast. The adsorbent was regenerated using 20 ml distilled water as an eluent at room temperature. A mere change in pH of the system resulted in rapid and appreciable desorption of the pollutant. The increase in pH to 7 reverses the surface charge of CMN-8 and electrostatic repulsion favours desorption of negatively charged chromium species. The adsorption-desorption processes of CMN-8 are controlled by pH driven surface charge of the adsorbent-adsorbate pair. The desorbed solution was evaluated using ICPMS to know the total chromium content in the desorbed solution and to detect the presence of leached iron from the adsorbent. The desorbed solution contained 94.25 mgL^{-1} of chromium species and very negligible iron (14.6 ppb). The Cr(VI) content was analysed spectrophotometrically using DPC reagent. The chromium species in the desorbed solution was identified to contain mainly Cr(III) – 87.67 mgL^{-1}, with a minor portion of Cr(VI)-6.58 mgL^{-1}. In practical setups, an additional

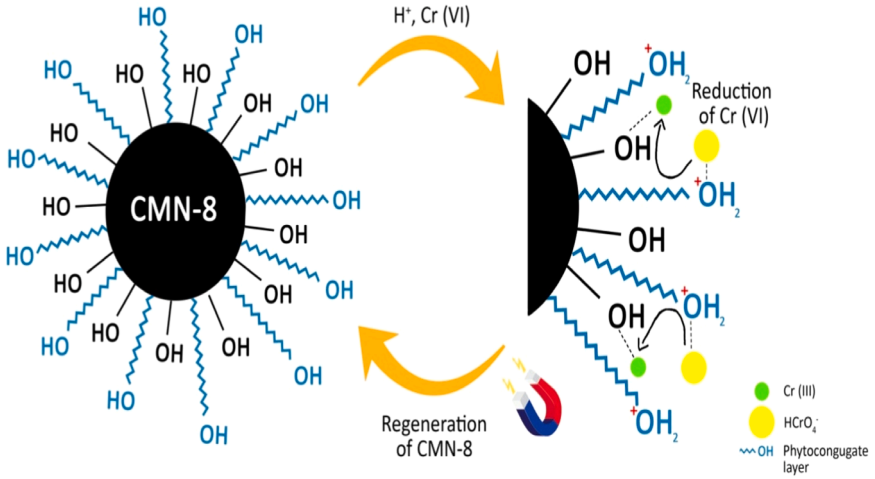

Fig. 11. Schematic representation of proposed mechanism for Cr(VI) removal and reduction by CMN-8.

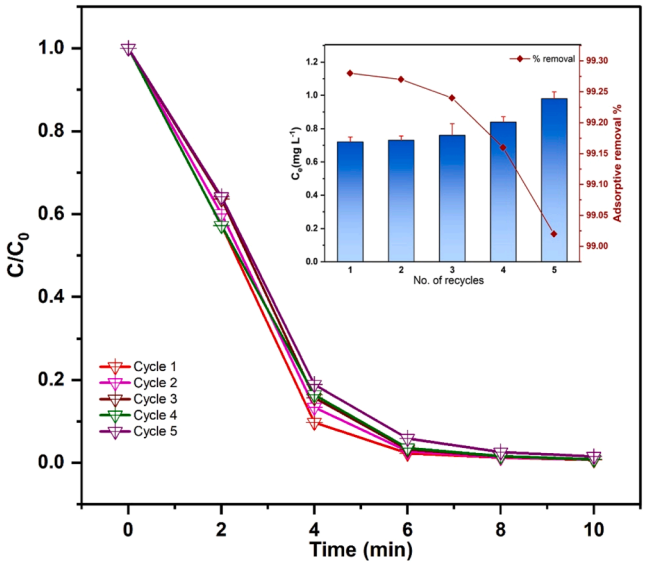

Fig. 12. Recyclability of CMN-8 up to 5 consecutive cycles.

process to separate/reduce the minor Cr(VI) concentration is required to use the recovered metal solution. The efficiency of CMN-8 for five consecutive adsorption-desorption cycles is illustrated in Fig. 12 Regenerated adsorbents displayed comparable adsorption capacity to fresh CMN-8. Magnetic collection of the adsorbent after each cycle eliminates possible loss of the material during the process and thus providing consistent adsorption efficiency. The invariable adsorption capacity also demonstrates the stability of CMN-8 resulted from the effective surface capping derived from flower extract.

4. Conclusions

The study resourced an invasive weed *Chromolaena odorata* for one-pot synthesis of superparamagnetic magnetite nanoparticles. The aqueous phytoextract containing high amounts of active secondary metabolites effectively reduced the metal ion and stabilized the nanoparticles formed. Assorted characterization techniques confirmed the formation of phyto-conjugated cubic inverse spinel Fe_3O_4. Superparamagnetic CMNs displayed rapid adsorptive performance towards toxic Cr(VI) species. Adsorption batch experiments revealed that CMN-8 was capable of removing ~99.28% of Cr(VI) from the aqueous effluents within 10 minutes. The adsorptive removal of Cr(VI) is initiated through electrostatic attraction between CMN-8 and the chromium species and the carbonaceous active sites on CMN-8 reduced Cr(VI) to less hazardous Cr(III). CMN-8 offered significant recyclability with minimal ionic interferences. Increase in pH of the simulated effluent above 4 impaired the adsorption of Cr(VI) onto CMN-8. Though crude plant extracts are fairly used in the synthesis of nanoparticles, the strategic use of hydrothermal and sonochemical assistance yielded us relatively monodispersed, fine, superparamagnetic, and stable magnetite nanoparticles. Upon scaling up the synthesis method can double up as effective weed control. Owing to the short contact period, superior efficiency, magnetic separation, and appreciable recyclability CMN-8 is a promising candidate for the removal and reduction of toxic Cr(VI) and is superior in many aspects compared to the reported methods. The work is green and economically sustainable in terms of the source materials, formed product, and its application.

Declaration of Competing Interest

The authors declare that they have no known competing financial interests or personal relationships that could have appeared to influence the work reported in this paper.

Data availability

No data was used for the research described in the article.

Acknowledgments

The author acknowledges the support provided by Dr. Pradeep A.K, Department of Botany, University of Calicut in identifying the collected plant. The research was supported by technical assistance from CSIF-University of Calicut, INUP CeNSE-IISc, Bangalore, SAIF- IIT Madras, PSGTECH-Coimbatore, STIC-CUSAT Kerala, DST-FIST Facility, Department of Chemistry, University of Calicut and KSCSTE Facility at CCS, Department of Chemistry, University of Calicut. One of the authors (JG) is thankful to CSIR-HRDG, Govt. of India for providing Senior Research Fellowship.

Supplementary materials

Supplementary material associated with this article can be found, in the online version, at doi:10.1016/j.materresbull.2022.112130.

References

[1] T.L. DesMarias, M. Costa, Mechanisms of chromium-induced toxicity, Curr. Opin. Toxicol. 14 (2019) 1–7.

[2] S. Prasad, K.K. Yadav, S. Kumar, N. Gupta, M.M. Cabral-Pinto, S. Rezania, N. Radwan, J. Alam, Chromium contamination and effect on environmental health and its remediation: A sustainable approaches, J. Environ. Manage. 285 (2021), 112174.

[3] V. Kumar, R.D. Parihar, A. Sharma, P. Bakshi, G.P.S. Sidhu, A.S. Bali, I. Karaouzas, R. Bhardwaj, A.K. Thukral, Y. Gyasi-Agyei, Global evaluation of heavy metal content in surface water bodies: a meta-analysis using heavy metal pollution indices and multivariate statistical analyses, Chemosphere 236 (2019), 124364.

[4] T.N. Baby, V. Vineethkumar, K. Shimod, C. Vishnu, S. Jayadevan, Heavy metal contamination in water sources of Thaliparamba municipality, Kerala, India, Radiat. Protect. Environ. 45 (1) (2022) 54.

[5] J.U. Ahmad, M.A. Goni, Heavy metal contamination in water, soil, and vegetables of the industrial areas in Dhaka, Bangladesh, Environ. Monit. Assess. 166 (1) (2010) 347–357.

[6] R. Acharya, A. Lenka, K. Parida, Magnetite modified amino group based polymer nanocomposites towards efficient adsorptive detoxification of aqueous Cr (VI): A review, J. Mol. Liq. 337 (2021), 116487.

[7] A. Behera, S. Mansingh, K.K. Das, K. Parida, Synergistic ZnFe2O4-carbon allotropes nanocomposite photocatalyst for norfloxacin degradation and Cr (VI) reduction, J. Colloid Interface Sci. 544 (2019) 96–111.

[8] P. Mishra, A. Behera, D. Kandi, K. Parida, Facile construction of a novel NiFe 2 O 4@ P-doped gC 3 N 4 nanocomposite with enhanced visible-light-driven photocatalytic activity, Nanoscale Adv. 1 (5) (2019) 1864–1879.

[9] D.K. Padhi, A. Baral, K. Parida, S. Singh, M.K. Ghosh, Visible light active single-crystal nanorod/needle-like α-MnO2@ RGO nanocomposites for efficient photoreduction of Cr (VI), J. Phys. Chem. C 121 (11) (2017) 6039–6049.

[10] S.P. Tripathy, S. Subudhi, S. Das, M.K. Ghosh, M. Das, R. Acharya, R. Acharya, K. Parida, Hydrolytically stable citrate capped Fe3O4@ UiO-66-NH2 MOF: a hetero-structure composite with enhanced activity towards Cr (VI) adsorption and photocatalytic H2 evolution, J. Colloid Interface Sci. 606 (2022) 353–366.

[11] K.E. Ukhurebor, U.O. Aigbe, R.B. Onyancha, W. Nwankwo, O.A. Osibote, H. K. Paumo, O.M. Ama, C.O. Adetunji, I.U. Siloko, Effect of hexavalent chromium on the environment and removal techniques: a review, J. Environ. Manage. 280 (2021), 111809.

[12] L. Zhou, Y. Duan, X. Xu, Facile preparation of amine-rich polyamidoamine (PAMAM) gel for highly efficient removal of Cr(VI) ions, Colloids Surf. A 579 (2019), 123685.

[13] R.S. Zambare, P.R. Nemade, Ionic liquid-modified graphene oxide sponge for hexavalent chromium removal from water, Colloids Surf. A 609 (2021), 125657.

[14] Q. Kong, J. Wei, Y. Hu, C. Wei, Fabrication of terminal amino hyperbranched polymer modified graphene oxide and its prominent adsorption performance towards Cr(VI), J. Hazard. Mater. 363 (2019) 161–169.

[15] S.O. Adio, M. Asif, A.-R.I. Mohammed, N. Baig, A.A. Al-Arfaj, T.A. Saleh, Poly (amidoxime) modified magnetic activated carbon for chromium and thallium adsorption: statistical analysis and regeneration, Process Saf. Environ. Prot. 121 (2019) 254–262.

[16] T. Phuengprasop, J. Sittiwong, F. Unob, Removal of heavy metal ions by iron oxide coated sewage sludge, J. Hazard. Mater. 186 (1) (2011) 502–507.

[17] P. Xu, G.M. Zeng, D.L. Huang, C.L. Feng, S. Hu, M.H. Zhao, C. Lai, Z. Wei, C. Huang, G.X. Xie, Use of iron oxide nanomaterials in wastewater treatment: a review, Sci. Total Environ. 424 (2012) 1–10.

[18] A.V. Samrot, C.S. Sahithya, J. Selvarani, S.K. Purayil, P. Ponnaiah, A review on synthesis, characterization and potential biological applications of superparamagnetic iron oxide nanoparticles, Curr. Res. Green Sustain. Chem. 4 (2021), 100042.

[19] J. Vidal-Vidal, J. Rivas, M. López-Quintela, Synthesis of monodisperse maghemite nanoparticles by the microemulsion method, Colloids Surf. A 288 (1-3) (2006) 44–51.

[20] A. Hassanjani-Roshan, M.R. Vaezi, A. Shokuhfar, Z. Rajabali, Synthesis of iron oxide nanoparticles via sonochemical method and their characterization, Particuology 9 (1) (2011) 95–99.

[21] F. Jiang, C.M. Wang, Y. Fu, R. Liu, Synthesis of iron oxide nanocubes via microwave-assisted solvolthermal method, J. Alloys Compd. 503 (2) (2010) L31–L33.

[22] L. Li, C. Luo, X. Li, H. Duan, X. Wang, Preparation of magnetic ionic liquid/chitosan/graphene oxide composite and application for water treatment, Int. J. Biol. Macromol. 66 (2014) 172–178.

[23] Y. Li, S. Zhu, Q. Liu, Z. Chen, J. Gu, C. Zhu, T. Lu, D. Zhang, J. Ma, N-doped porous carbon with magnetic particles formed in situ for enhanced Cr(VI) removal, Water Res. 47 (12) (2013) 4188–4197.

[24] T. Muthukumaran, J. Philip, Effect of phosphate and oleic acid capping on structure, magnetic properties and thermal stability of iron oxide nanoparticles, J. Alloys Compd. 689 (2016) 959–968.

[25] J. Tan, Y. Song, X. Huang, L. Zhou, Facile functionalization of natural peach gum polysaccharide with multiple amine groups for highly efficient removal of toxic hexavalent chromium (Cr(VI)) ions from water, ACS Omega 3 (12) (2018) 17309–17318.

[26] S. Zeng, J. Long, J. Sun, G. Wang, L. Zhou, A review on peach gum polysaccharide: hydrolysis, structure, properties and applications, Carbohydr. Polym. 279 (2022), 119015.

[27] S. Bishnoi, A. Kumar, R. Selvaraj, Facile synthesis of magnetic iron oxide nanoparticles using inedible Cynometra ramiflora fruit extract waste and their photocatalytic degradation of methylene blue dye, Mater. Res. Bull. 97 (2018) 121–127.

[28] L. Huang, X. Weng, Z. Chen, M. Megharaj, R. Naidu, Green synthesis of iron nanoparticles by various tea extracts: comparative study of the reactivity, Spectrochim. Acta Part A 130 (2014) 295–301.

[29] P.N.V.K. Pallela, S. Ummey, L.K. Ruddaraju, S. Gadi, C.S. Cherukuri, S. Barla, S. Pammi, Antibacterial efficacy of green synthesized α-Fe2O3 nanoparticles using Sida cordifolia plant extract, Heliyon 5 (11) (2019) e02765.

[30] B. Kumar, K. Smita, L. Cumbal, A. Debut, S. Galeas, V.H. Guerrero, Phytosynthesis and photocatalytic activity of magnetite (Fe3O4) nanoparticles using the Andean blackberry leaf, Mater. Chem. Phys. 179 (2016) 310–315.

[31] P.M. Mishra, G.K. Naik, A. Nayak, K.M. Parida, Facile synthesis of nano-structured magnetite in presence of natural surfactant for enhanced photocatalytic activity for water decomposition and Cr (VI) reduction, Chem. Eng. J. 299 (2016) 227–235.

[32] D.K. Padhi, T.K. Panigrahi, K. Parida, S.K. Singh, P.M. Mishra, Green synthesis of Fe3O4/RGO nanocomposite with enhanced photocatalytic performance for Cr(VI) reduction, phenol degradation, and antibacterial activity, ACS Sustain. Chem. Eng. 5 (11) (2017) 10551–10562.

[33] A. Rao, A. Bankar, A.R. Kumar, S. Gosavi, S. Zinjarde, Removal of hexavalent chromium ions by Yarrowia lipolytica cells modified with phyto-inspired Fe0/Fe3O4 nanoparticles, J. Contam. Hydrol. 146 (2013) 63–73.

[34] N.S. El-Gendy, H.N. Nassar, Biosynthesized magnetite nanoparticles as an environmental opulence and sustainable wastewater treatment, Sci. Total Environ. 774 (2021), 145610.

[35] P.O. Aigbedion-Atalor, M.D. Day, I. Idemudia, D.D. Wilson, I.D. Paterson, With or without you: stem-galling of a tephritid fly reduces the vegetative and reproductive performance of the invasive plant Chromolaena odorata (Asteraceae) both alone and in combination with another agent, BioControl 64 (1) (2019) 103–114.

[36] M.B. Taj, M.D. Alkahtani, A. Raheel, S. Shabbir, R. Fatima, S. Aroob, W. Alelwani, N. Alahmadi, M. Abualnaja, S. Noor, Bioconjugate synthesis, phytochemical analysis, and optical activity of NiFe2O4 nanoparticles for the removal of ciprofloxacin and Congo red from water, Sci. Rep. 11 (1) (2021) 1–19.

[37] E.A. Ainsworth, K.M. Gillespie, Estimation of total phenolic content and other oxidation substrates in plant tissues using Folin–Ciocalteu reagent, Nat. Protoc. 2 (4) (2007) 875–877.

[38] C.-C. Chang, M.-H. Yang, H.-M. Wen, J.-C. Chern, Estimation of total flavonoid content in propolis by two complementary colorimetric methods, J. Food Drug Anal. 10 (3) (2002).

[39] A. Lace, D. Ryan, M. Bowkett, J. Cleary, Chromium monitoring in water by colorimetry using optimised 1, 5-diphenylcarbazide method, Int. J. Environ. Res. Public Health 16 (10) (2019) 1803.

[40] H. Cui, Y. Liu, W. Ren, Structure switch between α-Fe2O3, γ-Fe2O3 and Fe3O4 during the large scale and low temperature sol–gel synthesis of nearly monodispersed iron oxide nanoparticles, Adv. Powder Technol. 24 (1) (2013) 93–97.

[41] E.B. Denkbaş, E. Çelik, E. Erdal, D. Kavaz, Ö. Akbal, G. Kara, C. Bayram, Chapter 9 - Magnetically based nanocarriers in drug delivery, in: A.M. Grumezescu (Ed.), Nanobiomaterials in Drug Delivery, William Andrew Publishing, 2016, pp. 285–331.

[42] A. Ricci, K.J. Olejar, G.P. Parpinello, P.A. Kilmartin, A. Versari, Application of fourier transform infrared (FTIR) spectroscopy in the characterization of tannins, Appl. Spectrosc. Rev. 50 (5) (2015) 407–442.

[43] X. Wang, Y. Zhao, X. Jiang, L. Liu, X. Li, H. Li, W. Liang, In-situ self-assembly of plant polyphenol-coated Fe3O4 particles for oleaginous microalgae harvesting, J. Environ. Manage. 214 (2018) 335–345.

[44] A. Rajan, M. Sharma, N.K. Sahu, Assessing magnetic and inductive thermal properties of various surfactants functionalised Fe3O4 nanoparticles for hyperthermia, Sci. Rep. 10 (1) (2020) 1–15.

[45] K.S. Sing, R.T. Williams, Physisorption hysteresis loops and the characterization of nanoporous materials, Adsorpt. Sci. Technol. 22 (10) (2004) 773–782.

[46] F.N. Eze, T.J. Jayeoye, Chromolaena odorata (Siam weed): a natural reservoir of bioactive compounds with potent anti-fibrillogenic, antioxidative, and cytocompatible properties, Biomed. Pharmacother. 141 (2021), 111811.

[47] M. Elhabiri, C. Carrër, F. Marmolle, H. Traboulsi, Complexation of iron(III) by catecholate-type polyphenols, Inorg. Chim. Acta 360 (1) (2007) 353–359.

[48] Z. Kozakova, I. Kuritka, N.E. Kazantseva, V. Babayan, M. Pastorek, M. Machovsky, P. Bazant, P. Saha, The formation mechanism of iron oxide nanoparticles within the microwave-assisted solvothermal synthesis and its correlation with the structural and magnetic properties, Dalton Trans. 44 (48) (2015) 21099–21108.

[49] G. Dognani, P. Hadi, H. Ma, F.C. Cabrera, A.E. Job, D.L.S. Agostini, B.S. Hsiao, Effective chromium removal from water by polyaniline-coated electrospun adsorbent membrane, Chem. Eng. J. 372 (2019) 341–351.

[50] A. Gallo-Cordova, M.d.P. Morales, E. Mazarío, Effect of the surface charge on the adsorption capacity of chromium (VI) of iron oxide magnetic nanoparticles prepared by microwave-assisted synthesis, Water 11 (11) (2019) 2372.

[51] S.R. Chowdhury, E.K. Yanful, A.R. Pratt, Chemical states in XPS and Raman analysis during removal of Cr (VI) from contaminated water by mixed maghemite–magnetite nanoparticles, J. Hazard. Mater. 235 (2012) 246–256.

[52] F. Zhu, S. Ma, T. Liu, X. Deng, Green synthesis of nano zero-valent iron/Cu by green tea to remove hexavalent chromium from groundwater, J. Cleaner Prod. 174 (2018) 184–190.

[53] L. Castro, M.L. Blázquez, F. González, J.A. Muñoz, A. Ballester, Heavy metal adsorption using biogenic iron compounds, Hydrometallurgy 179 (2018) 44–51.

[54] S. Chatterjee, S. Mahanty, P. Das, P. Chaudhuri, S. Das, Biofabrication of iron oxide nanoparticles using manglicolous fungus Aspergillus niger BSC-1 and removal of Cr (VI) from aqueous solution, Chem. Eng. J. 385 (2020), 123790.

[55] F.-X. Dong, L. Yan, X.-H. Zhou, S.-T. Huang, J.-Y. Liang, W.-X. Zhang, Z.-W. Guo, P.-R. Guo, W. Qian, L.-J. Kong, Simultaneous adsorption of Cr (VI) and phenol by biochar-based iron oxide composites in water: performance, kinetics and mechanism, J. Hazard. Mater. 416 (2021), 125930.
[56] G. Sarojini, S. Venkatesh Babu, N. Rajamohan, P. Senthil Kumar, M. Rajasimman, Surface modified polymer-magnetic-algae nanocomposite for the removal of chromium- equilibrium and mechanism studies, Environ. Res. 201 (2021), 111626.
[57] H. Zou, J. Zhao, F. He, Z. Zhong, J. Huang, Y. Zheng, Y. Zhang, Y. Yang, F. Yu, M. A. Bashir, Ball milling biochar iron oxide composites for the removal of chromium (Cr (VI)) from water: performance and mechanisms, J. Hazard. Mater. 413 (2021), 125252.
[58] S. Poulin, R. Franca, L. Moreau-Bélanger, E. Sacher, Confirmation of X-ray photoelectron spectroscopy peak attributions of nanoparticulate iron oxides, using symmetric peak component line shapes, J. Phys. Chem. C 114 (24) (2010) 10711–10718.
[59] A.T. Mathew, S. Hegde, K. Akshaya, P. Kannan, A. Varghese, G. Hegde, MnO2-Pi on biomass derived porous carbon for electro-catalytic oxidation of pyridyl carbinol, J. Electrochem. Soc. 167 (15) (2020), 155513.
[60] S. Riaz, A. Akbar, S. Naseem, Ferromagnetic effects in Cr-doped Fe 2 O 3 thin films, IEEE Trans. Magn. 50 (8) (2014) 1–4.